Structural basis of inhibition of Mycobacterium tuberculosis DprE1 by benzothiazinone inhibitors

Batt, Sarah M; Jabeen, Talat; Bhowruth, Veemal; Quill, Lee; Lund, Peter A; Eggeling, Lothar; Alderwick, Luke J; Fütterer, Klaus; Besra, Gurdyal S

DOI:
10.1073/pnas.1205735109

Document Version
Publisher's PDF, also known as Version of record

Citation for published version (Harvard):
Batt, SM, Jabeen, T, Bhowruth, V, Quill, L, Lund, PA, Eggeling, L, Alderwick, LJ, Fütterer, K & Besra, GS 2012, 'Structural basis of inhibition of Mycobacterium tuberculosis DprE1 by benzothiazinone inhibitors', *National Academy of Sciences. Proceedings*, vol. 109, no. 28, pp. 11354-9. https://doi.org/10.1073/pnas.1205735109

Structural basis of inhibition of *Mycobacterium tuberculosis* DprE1 by benzothiazinone inhibitors

Sarah M. Batt[a], Talat Jabeen[a], Veemal Bhowruth[a], Lee Quill[a], Peter A. Lund[a], Lothar Eggeling[b], Luke J. Alderwick[a,1], Klaus Fütterer[a,1], and Gurdyal S. Besra[a,1]

[a]School of Biosciences, University of Birmingham, Edgbaston, Birmingham B15 2TT, United Kingdom; and [b]Institut für Biotechnologie I, Forschungszentrum Jülich, D-52428 Jülich, Germany

Edited* by Michael B. Brenner, Brigham and Women's Hospital and Harvard Medical School, Boston, MA, and approved June 4, 2012 (received for review April 4, 2012)

Resistance against currently used antitubercular therapeutics increasingly undermines efforts to contain the worldwide tuberculosis (TB) epidemic. Recently, benzothiazinone (BTZ) inhibitors have shown nanomolar potency against both drug-susceptible and multidrug-resistant strains of the tubercle bacillus. However, their proposed mode of action is lacking structural evidence. We report here the crystal structure of the BTZ target, FAD-containing oxidoreductase *Mycobacterium tuberculosis* DprE1, which is essential for viability. Different crystal forms of ligand-free DprE1 reveal considerable levels of structural flexibility of two surface loops that seem to govern accessibility of the active site. Structures of complexes with the BTZ-derived nitroso derivative CT325 reveal the mode of inhibitor binding, which includes a covalent link to conserved Cys387, and reveal a trifluoromethyl group as a second key determinant of interaction with the enzyme. Surprisingly, we find that a noncovalent complex was formed between DprE1 and CT319, which is structurally identical to CT325 except for an inert nitro group replacing the reactive nitroso group. This demonstrates that binding of BTZ-class inhibitors to DprE1 is not strictly dependent on formation of the covalent link to Cys387. On the basis of the structural and activity data, we propose that the complex of DrpE1 bound to CT325 is a representative of the BTZ-target complex. These results mark a significant step forward in the characterization of a key TB drug target.

mycobacterial cell wall | X-ray crystallography | multi drug resistance | arabinan | decaprenylphosphoryl-D-arabinose

For the past several decades, treatment of active tuberculosis (TB) infections has relied on a relatively small set of chemotherapeutic agents, including the widely used front-line drugs isoniazid, ethambutol, rifampicin, and pyrazinamide (1). The lack of novel inhibitors of adequate efficacy has favored the emergence of multidrug-resistant (MDR) and extensive drug-resistant (XDR) strains of the tubercle bacillus, drastically increasing the cost and duration of treatment and threatening to undermine World Health Organization-led efforts to contain the global TB pandemic (2, 3). Responding to the urgent need for new antibiotics, partnerships between academic institutions, research charities, and industry have been able to feed a modest pipeline of drug leads, with two candidates currently in phase III clinical trials (4). However, more recently nitro-benzothiazinones (BTZs) have emerged as a promising class of inhibitors, effective against both drug-susceptible and MDR/XDR strains of *Mycobacterium tuberculosis* at significantly lower minimum inhibitory concentrations (MICs) than either isoniazid or rifampicin, in combination with reduced toxicity (5, 6). The most potent compound in this series to date, BTZ043 (Scheme 1*A*), has an MIC of 1 ng/mL against *M. tuberculosis*, 20-fold less than that of isoniazid (5). A structurally related set of compounds, dinitrobenzamides (DNBs), which includes *N*-(2-(4-methoxyphenoxy) ethyl)-3,5-dinitrobenzamide (DNB1; Scheme 1*A*), have likewise shown potency against XDR strains combined with low toxicity (7).

BTZ and related compounds inhibit the conversion of decaprenylphosphoryl-β-D-ribose (DPR) to decaprenylphosphoryl-β-D-arabinofuranose (DPA; Scheme 1*B*), a precursor of mycobacterial cell wall arabinan. This two-step epimerization reaction is catalyzed by the joint or successive action of the FAD-containing oxidoreductase DprE1 (Rv3790) and the NADH-dependent reductase DprE2 (Rv3791) (Scheme 1*B*) (8). DPA is the sole known donor substrate for a series of membrane-embedded arabinosyltransferases, including the ethambutol targets EmbC, EmbA, and EmbB (9). Essentiality of DPA supply and lack of alternative synthetic pathways position DprE1, which is highly conserved in mycobacteria (Fig. S1*A*), and DprE2 at a critical intersection of cell wall biosynthesis, a notion confirmed by transposon mutagenesis (10, 11). This situation has led some to speak of DprE1 as a magic drug target (1).

BTZ and DNB class inhibitors both contain a central benzene ring carrying a nitro group at position 3 (Scheme 1*A*). Inhibition of DprE1 by BTZ/DNB inhibitors has been shown to require conversion of the nitro to a nitroso group, proposed to form a semimercaptal linkage with a conserved cysteine in the active site of DprE1 (Cys387 in *M. tuberculosis*) (12, 13). There has been speculation that BTZ and DNB inhibitors require activation by a separate nitroreductase (14), but more recently it has been proposed that DprE1 itself is able to activate BTZ in a substrate-dependent fashion, prompting their characterization as suicide inhibitors (13).

Efforts to structurally characterize *M. tuberculosis* DprE1 and its interaction with inhibitors were hampered by the failure to obtain sufficient amounts of soluble recombinant protein. We have been able to overcome this roadblock, facilitating crystallization and structure determination of this target. Herein, we report the crystal structure of *M. tuberculosis* DprE1, both in the ligand-free form and bound to the BTZ-derived inhibitors CT325 and CT319 (12).

Results

Coexpression with Mycobacterial Chaperonin Yields Soluble Recombinant *M. tuberculosis* DprE1. Exploring coexpression with chaperones we found that small amounts of soluble DprE1 could be obtained using the *Escherichia coli* Tuner strain (Fig. S2*A*).

Author contributions: S.M.B., L.J.A., K.F., and G.S.B. designed research; S.M.B., T.J., L.Q., L.J.A., and K.F. performed research; V.B., P.A.L., and L.E. contributed new reagents/analytic tools; S.M.B. and K.F. analyzed data; and K.F. and G.S.B. wrote the paper.

The authors declare no conflict of interest.

*This Direct Submission article had a prearranged editor.

Freely available online through the PNAS open access option.

Data deposition: The atomic coordinates and structure factors reported in this paper have been deposited in the Protein Data Bank, www.pdb.org (PDB ID codes 4FDN, 4FDO, 4FDP, 4FEH, and 4FF6).

[1]To whom correspondence may be addressed. E-mail: g.besra@bham.ac.uk, l.alderwick@bham.ac.uk, or k.futterer@bham.ac.uk.

This article contains supporting information online at www.pnas.org/lookup/suppl/doi:10.1073/pnas.1205735109/-/DCSupplemental.

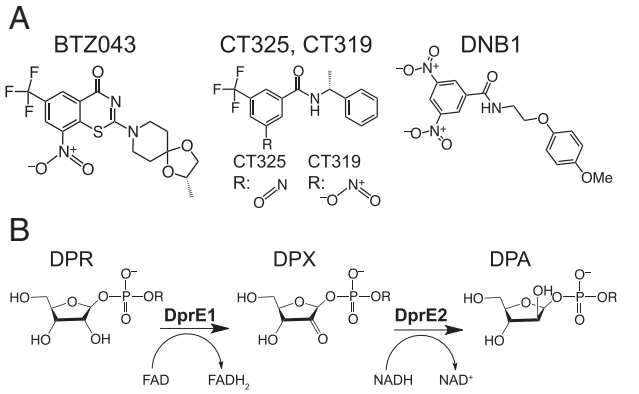

Scheme 1. Epimerization reaction of DPR to DPA and chemical structures of inhibitors. (*A*) Chemical structures of BTZ043 (5), CT325 and CT319 (12), and DNB1 (7). (*B*) Conversion of DPR to DPA involves oxidation and subsequent reduction of the C2′ hydroxyl via a keto-intermediate (DPX). Relevant enzymes and redox cofactors are indicated.

The amount of DprE1 was consistently less than that of chaperonin *E. coli* GroEL, and attempts to separate the two products by chromatography were not successful. Coexpressing DprE1 with the mycobacterial GroEL homolog Cpn60.1 and the cochaperonin *E. coli* GroES (Fig. S2*B*) gave similarly disappointing results. However, coexpression with *M. tuberculosis* Cpn60.2 and *E. coli* GroES led to a significant increase of soluble DprE1 that could be readily separated from the chaperone component by Ni-NTA and ion exchange chromatography, yielding ∼5 mg of pure DprE1 from a 2-L culture (Fig. S2 *C* and *D*). Although no FAD was added to cell lysates or purification buffers, concentrated and crystallized DprE1 showed the characteristic intense yellow color of a FAD-containing protein in the oxidized state.

Crystallographic Structure Determination and Overall Structure of DprE1. Crystallization screens of purified *M. tuberculosis* DprE1 resulted in hits for several reservoir conditions, with crystals in space group symmetries $P2_1$ or $P6_4$ (Tables S1 and S2). Phases for the structure of ligand-free DprE1 were determined by single-wavelength anomalous diffraction of an ytterbium-derivative crystal of monoclinic DprE1 (two molecules per asymmetric unit; Fig. S3 *A* and *B* and Table S1). Crystals of DprE1 in complex with *R*-3-(nitroso)-*N*-(1-phenylethyl)-5-(trifluoromethyl) benzamide [CT325 (12)] were obtained both in the hexagonal and monoclinic crystal forms, providing crystallographically independent views of the mode of inhibitor binding. In addition we obtained crystals in complex with *R*-3-(nitro)-*N*-(1-phenylethyl)-5-(trifluoromethyl) benzamide [CT319 (12)], which carries an NO_2 instead of the NO ring substituent of CT325.

The model of the hexagonal crystal form in complex with CT319 comprises residues 7–461, with one disordered region (residues 268 and 298), whereas the ligand-free forms and the CT325 complex include two disordered regions in the chain (Figs. 1 and 2 and Fig. S3*C*). The overall structure of DprE1 resembles closely that of FAD-containing alditol oxidase from *Streptomyces coelicolor* (Protein Data Bank ID code 2VFR, 20% sequence identity, rmsd 3.0 Å for 374 aligned residues; Fig. S3*D*) (15), its closest structural neighbor according to distance matrix alignment using DALI (16). Alditol oxidase is a representative of the vanillyl-alcohol oxidase (VAO) family of oxidoreductases (17, 18).

The structure of DprE1 can be divided into the FAD-binding domain (residues 7–196, 413–461) and the substrate-binding domain (residues 197–412) (Fig. 1*A* and Fig. S3*C*). The FAD-binding domain consists of an α+β fold, including two small

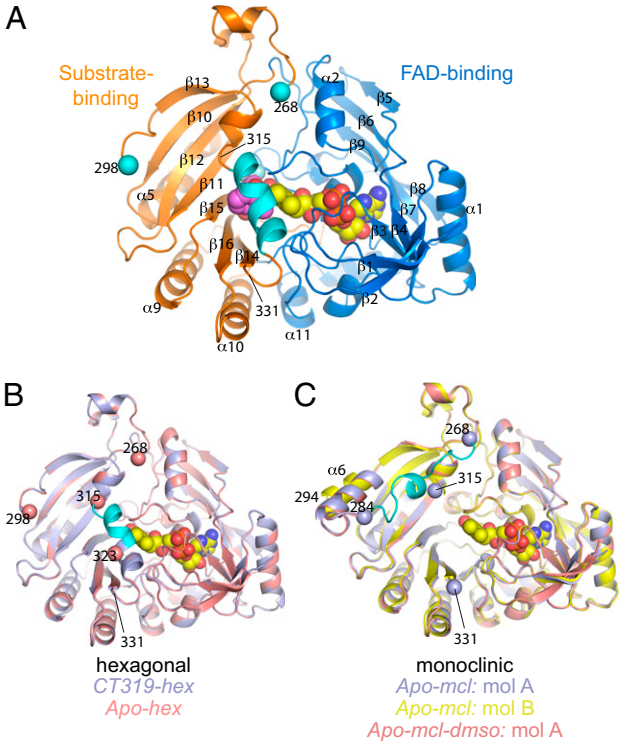

Fig. 1. Fold of *M. tuberculosis* DprE1 and structural plasticity of surface loops 269–297 and 316–330. (*A*) Ribbon diagram of DprE1 in the hexagonal crystal form bound to the ligand CT319. FAD is shown in spheres (yellow carbons), whereas CT319 is shown in violet spheres. Spheres in cyan indicate the boundaries of the disordered region of residues 269–297. In the CT319-bound form, residues 317–327 (cyan) form a helix. (*B*) Superposition of ligand-free (*Apo-hex*, salmon-colored) and inhibitor-bound (*CT319-hex*, light blue) DprE1 of the hexagonal crystal form. The region of residues 316–322 (cyan) becomes ordered upon ligand binding. (*C*) Superposition of structures obtained from monoclinic crystals (*Apo-mcl*: molecules A and B; *Apo-mcl-dmso*: molecule A). The region of residues 268–283 (cyan) is ordered only in molecule A of *Apo-mcl-dmso*.

β-sheets (strands β1–β4 and β5–β9, respectively), and several helices (α1–α4 and α11–α13). The cofactor is deeply buried in the FAD-binding domain, with the isoalloxazine positioned at the interface to the substrate-binding domain. In comparison with the structure of alditol oxidase (15) and several other structural homologs of DprE1, the conformation of FAD and its immediate protein environment are highly conserved. However, in DprE1 there is no covalent link between FAD and the protein, as is typical for VAO enzymes (17). The substrate-binding domain consists of an extended, antiparallel β-sheet (strands β10–β16) that faces the domain interface with flavin at the center, decorated by three extended helices (α5, α9, and α10) on the back. This domain includes, in the ligand-free and CT325-bound states, the two disordered regions.

The monoclinic and hexagonal crystal forms both display an apparent dimer of DprE1 (Fig. S4*A*). Independent of symmetry, dimerization is mediated by a twofold rotation axis that aligns strands β5 (residues 80–84) of two copies of DprE1, related by either space group symmetry (hexagonal lattice) or noncrystallographic symmetry (monoclinic lattice), respectively. The dimerization interface (buried solvent-accessible surface ∼340 $Å^2$) is stabilized by four main chain–main chain hydrogen bonds and hydrophobic interactions between side chains of residues Ile80, Ile83, and Phe108 (Fig. S4*B*). However, in sedimentation velocity experiments we find a single monomer peak, suggesting that DprE1 does not dimerize appreciably in solution (Fig. S4*C*).

MICROBIOLOGY

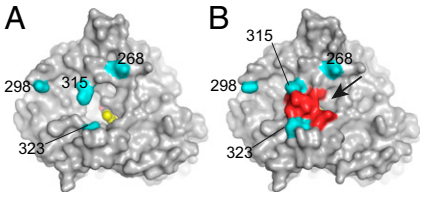

Fig. 2. Molecular surfaces of ligand-free and inhibitor-bound DprE1 (hexagonal form). (*A*) Ligand-free DprE1 (*Apo-hex*), with FAD shown as spheres (yellow carbons). The boundaries of the disordered regions are marked in cyan, and the corresponding residue number is indicated. (*B*) CT319-bound DprE1 (*CT319-hex*), where ordering of residues 316–322 (red surface) leads to shielding of the active site from solvent, except for an access channel to the *re* side of flavin (arrow).

Structural Flexibility of DprE1. Electron density of both crystal forms obtained for ligand-free DprE1 reveal disorder of two surface loops in the substrate-binding domain. As a consequence of the disorder, the active site is wide open in the ligand-free form of the enzyme (Fig. 2*A*). At a maximum, residues 269–297 and 316–330 are lacking electron density, but the degree of disorder or extent of the apparent gaps varies between the monoclinic and hexagonal crystal forms. In the hexagonal form of ligand-free DprE1, the first region is disordered between residues 269 and 297, and the second region lacks density for residues 316–322 (Fig. 1*B*). In the monoclinic crystal form, the density gap in the second region is considerably larger, affecting residues 316–330 (Fig. 1*C*). In contrast, the density gap in the first region is smaller than in hexagonal crystals but varies between the two crystallographically distinct molecules of monoclinic DprE1: molecule A is lacking density for residues 269–283, whereas in molecule B this gap extends from 269 to 293 (Fig. 1*C*). As a result, helix α6 (residues 292–298) only forms fully in molecule A of monoclinic DprE1, whereas it appears as a two-turn fragment in molecule B (Fig. 1*C*) and is altogether absent from the structural model of hexagonal DprE1 (Fig. 1*B*).

However, there are two conditions under which we observe ordering of region one or region two, but not both simultaneously. In the density for crystal *Apo-mcl-dmso*, the chain can be completely traced between residues 268 and 284 for molecule A (trace in cyan in Fig. 1*C*) but not for molecule B. The peptide chain of this region is vaulting over the β-sheet of the substrate-binding domain. Contacts with a symmetry-related copy of molecule A in the center of this loop help stabilize this particular conformation. Complete ordering of the second region (residues 316–330) is observed in hexagonal crystal of the DprE1:CT319 complex, where residues 316–322 become ordered when CT319 is bound (trace in cyan in Fig. 1*B*, red surface in Fig. 2*B*, and Fig. S5 *A* and *B*). As result, residues 317–327 form a three-turn helix (Fig. 1*A*, trace in cyan), although it does not maintain strict α-helical geometry. Unit cell parameters and crystal symmetry are unchanged between the ligand-free and the CT325- and CT319-bound forms of hexagonal DprE1, despite different reservoir conditions (Table S2). We, therefore, attribute ordering of residues 316–322 to binding of CT319, the position of which in the active site differs subtly but distinctly from that of CT325 (Fig. S5*C*).

Structures of the Complexes with BTZ Derivatives CT325 and CT319. Although fluorescence-based ligand-binding experiments (Fig. S6*A*) demonstrated binding of the inhibitor BTZ043 (5) to DprE1, crystals grown in the presence of BTZ043 did not reveal a bound ligand. Trefzer et al. (13) had suggested that formation of the covalent complex between BTZ043 and DprE1 requires prior conversion of the nitro group to the nitroso form. To circumvent the need for inhibitor activation, we synthesized the nitroso-benzothiazinone CT325 (12) for cocrystallization experiments.

We obtained crystals of the DprE1:CT325 complex in both the hexagonal and monoclinic crystal forms (*CT325-hex3* and *CT325-mcl*; Table S1) and recorded diffraction data to resolutions of 2.4 and 2.6 Å (CuKα), respectively. A σ_A-weighted Fo-Fc difference density map, calculated with model phases before including the ligand in the model, displays prominent density between flavin and Cys387, the residue postulated to be critical for BTZ-mediated inhibition of DprE1 activity and BTZ-dependent cessation of mycobacterial growth (5) (Fig. 3 *A* and *B*). We observe bridging density between this cysteine and the density enveloping the inhibitor model, evidence for the formation of a covalent bond between CT325 and Cys387 in both crystal forms. However, the conformation of the

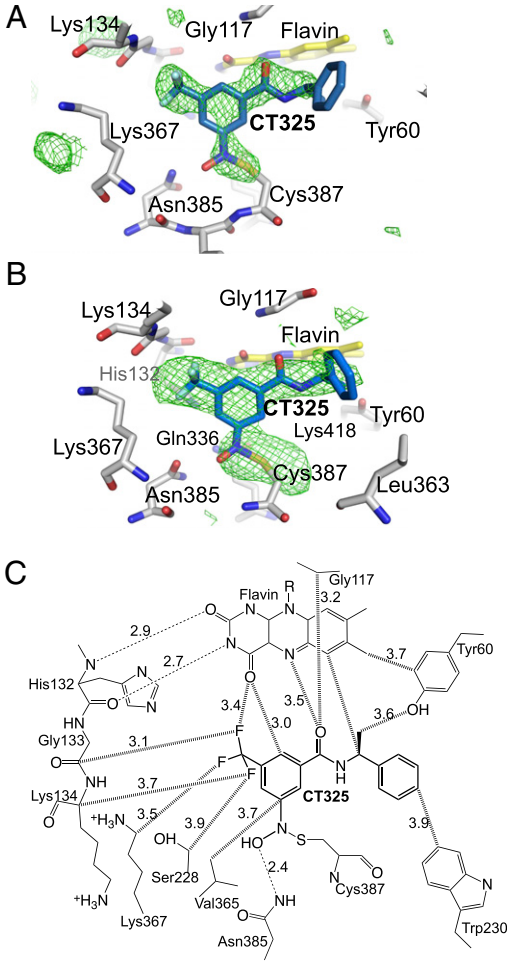

Fig. 3. Mode of binding of the nitroso derivative CT325 in the active site of DprE1. (*A*) Stick model of FAD (yellow carbons), CT325 (blue carbons), and selected protein residues (gray carbon) situated within a 4-Å cutoff distance from the inhibitor. The σ_A-weighted F_O-F_C density map was calculated on the basis of model phases before incorporation of CT325 in the structural model and is contoured at 3.0σ above the mean. The structure was refined including a covalent link between Cys387 and CT325. (*B*) Analogous view to *A*, showing the active site of molecule A in monoclinic crystal *CT325-mcl*. The σ_A-weighted F_O-F_C density map is contoured at 2.0σ above the mean. (*C*) Schematic representation of CT325-protein contacts in the active site of DprE1. Thick, hashed lines indicate noncovalent interactions (van der Waals, hydrophobic), with interatomic distances given in units of Å, whereas dashed lines indicate hydrogen bonds. For graphical simplicity, only contacts of 4 Å or shorter have been included, and Gln336 has been omitted from the view.

phenylethyl group remained undefined in the CT325 complexes. While attempting to obtain diffraction data of the DprE1:CT325 complex, we noticed that for some crystals the bridging density between CT325 and Cys387 was notably absent, but the whole of the inhibitor molecule was defined by electron density, including the terminal phenylethyl group. We suspected that the reactive nitroso group was unstable and may have reverted to the more stable NO_2 state before binding to the protein, preventing formation of the covalent link to Cy387. To test this assumption we generated crystals of CT319-bound DprE1, which led to a noncovalent complex and ordering of the loop region encompassing residues 316–322 over the active site (Fig. S5*A*). As a result of the ordered state of residues 316–330, the active site is shielded from bulk solvent (Fig. 2*B*), whereas in the crystals of the DprE1:CT325 complex, the 316–330 loop region remains in the disordered state.

The consistent density features obtained from crystals in different crystal forms allow one to unequivocally position CT325 in the active site. The inhibitor adopts an extended conformation, running parallel to the isoalloxazine. The trifluoromethyl moiety packs against the backbone of residues 132–134, forming van der Waals interactions with Gly133 and Lys134 (contact distances between 3.3 Å and 3.9 Å; Fig. 3*C* and Fig. S7*A*), with additional van der Waals contacts to the side chains of His132, Ser228, and Lys367. The central benzamide group primarily interacts with the flavin (contact distances between 3.0 Å and 3.5 Å), with Gly117 (3.2 Å), and with the side chain of Val365 (shortest contact 3.7 Å). In addition the NO group forms a strong H-bond (2.4 Å) with the amide of Asn385. Compared with the ligand-free and CT319-bound state, the side chain of Cys387 is rotated by 180° about the Cα–Cβ bond, facilitating the covalent bond to the nitroso group, consistent with a previous prediction (12). The terminal phenylethyl group is disordered in the CT325-bound complex but well ordered for CT319, in which case the benzene ring occupies a hydrophobic cavity formed by Leu363 and Val365 in strand β16, Trp230 in strand β11, and by Leu317 and Phe320 in the "316–322" loop (Fig. S7*B*). In the absence of loop ordering, the cavity applies fewer constraints on the orientation of the phenyl ring, and it is plausible that the terminal benzene ring can assume variable orientations.

CT325 Inhibits Epimerization of DPR to DPA. Although CT319-dependent inhibition of DprE1 had been previously demonstrated for the *Mycobacterium smegmatis* ortholog (12), activity data were not available to us for CT325. Incubating ^{14}C-labeled decaprenylphosphoryl-β-D-ribose (^{14}C-DPR) with purified *M. tuberculosis* DprE1 and DprE2 and analyzing reaction products by TLC, we observe almost complete conversion of DPR to DPA (Fig. 4*A*). When incubated with DprE1 alone, the DPR band is reduced in intensity, and a distinct band appears below the DPR band, representing the keto-intermediate DPX (Fig. 4 *A* and *B* and Scheme 1*A*). No DPA is generated under these conditions. Adding CT325 to the reaction mixture represses DPX formation in a dose-dependent fashion (Fig. 4*B*), confirming inhibition of DprE1 activity by this inhibitor. Adding CT325 to a reaction mixture containing both DprE1 and DprE2 represses conversion to DPA (Fig. 4*A*). Furthermore, growth of the nonpathogenic surrogate organisms *M. smegmatis* and *Mycobacterium bovis* bacillus Calmette–Guérin are inhibited by CT325, with EC_{50} values of 10.4 and 4.6 μg/mL, respectively (Fig. 4*C*).

In agreement with previous studies in which activity of BTZ043 was assessed against *M. smegmatis* DrpE1 (5, 12, 13), we find that BTZ043 inhibits DPR to DPX conversion of *M. tuberculosis* DprE1 (Fig. 4*A*). Thus, we are able to show that that CT325 replicates the activity of BTZ043, in terms of inhibition of conversion of DPR to DPX (Fig. 4*A*) and in terms of whole-cell activity (Fig. 4*C*), albeit with significantly lower potency than BTZ043.

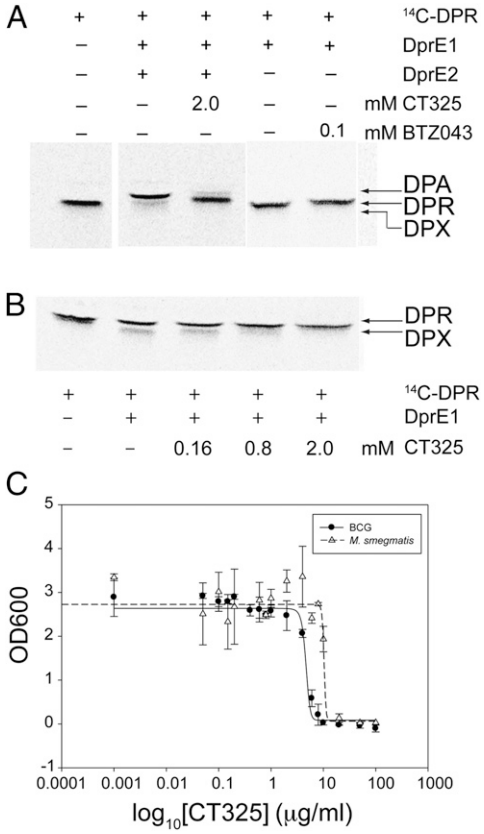

Fig. 4. Assays probing inhibition of DprE1 and whole-cell activity of CT325. (*A*) ^{14}C-labeled DPR was incubated with DprE1 and DprE2, and epimerization of DPR to DPA monitored by TLC. (*B*) As in *A*, but ^{14}C-labeled substrate was incubated with DprE1 alone, and conversion to the keto-intermediate DPX was monitored. (*C*) CT325-induced inhibition of growth in batch cultures of *M. bovis* bacillus Calmette–Guérin and *M. smegmatis*, monitored for 10 d and 40 h, respectively, by measuring absorbance at 600 nm. SDs are derived from two independent experiments.

Discussion

The recent controversy surrounding the report of a "totally drug resistant" strain of *M. tuberculosis* in India (19) illustrates the high stakes involved in the effort to control the TB pandemic, in particular because this burden is carried primarily by resource-limited health care systems in the developing world. Thus, the discovery of benzothiazinones and dinitrobenzamides as novel classes of potent inhibitors, effective against both drug-susceptible and MDR/XDR forms of TB, and the identification of their target—DprE1—are significant steps forward.

Epimerization of DPR is the final step of DPA synthesis, which involves the conversion of glucose to ribose-5-phosphate via the pentose phosphate pathway, followed by synthesis of phosphoribose-diphosphate (pRpp), nucleophilic replacement of pyrophosphate by decaprenyl-phosphate, and removal of the 5′-phosphate to yield DPR (20). Although not firmly established, it is likely that after attachment of the decaprenyl group, the DPA precursor compounds are anchored into the cell membrane. This raises the question of how DprE1 gains access to substrate. DprE1 may need to be able to partially or wholly sequester the decaprenyl moiety of the substrate. The wide-open active site of ligand-free DprE1 and the two flexible loops contrast with the narrow, funnel-like access channel to the active site in the known structures of ligand-free VAO enzymes, for instance in alditol oxidase (Fig. S7*C*). Therefore, it seems plausible to invoke a link between flexibility of these loops and DPR binding.

We propose that the structure of CT325-bound DprE1 is a representative of the activated BTZ-target complex. The structure and activity data demonstrate that CT325 binds to DprE1 and that this interaction interferes with the conversion of DPR to DPX in a dose-dependent fashion (Fig. 4*B*). We have not shown explicitly that inhibition of DprE1 by CT325 compromises cell wall arabinan, but the suppression of DPR to DPA conversion (Fig. 4*A*) and CT325's whole-cell activity against *M. smegmatis* and *M. bovis* bacillus Calmette–Guérin (Fig. 4*C*) provides indirect evidence for such an effect.

Covalent binding of BTZ043 to DprE1 has been shown to be dependent on Cys387: substitutions by Gly or Ser at this sequence position resulted in resistance to BTZ or DNB inhibitors (5, 12). The Fo-Fc difference electron density of the inhibitor-bound structure of hexagonal and monoclinic DprE1 unequivocally indicate a covalent link between CT325 and Cys387 (Fig. 3 *A* and *B*), and the shape of the bridging density is consistent with a semimercaptal linkage. Density for the trifluoromethyl group (8.7σ in *CT325-mcl*, 6.6 σ in *CT325-hex3*), the electron-withdrawing ring substituent, is seen consistently in all CT325 complex structures we obtained. Thus, the trifluoromethyl seems to be a second key determinant of CT325 binding, which together with the covalent bond and the spatial constraints imposed by the active site unequivocally position the ligand on the *si* side of flavin. The terminal phenylethyl moiety is only defined in the noncovalent complex with CT319. In the latter complex, ligand binding is accompanied by ordering of the second surface loop (residues 316–322), which closes the active site and provides additional contacts to stabilize the phenylethyl in a defined conformation (Figs. S5*A* and S7*B*). Apart from the covalent link to Cys387, van der Waals interactions dominate the network of noncovalent contacts between enzyme and CT325 (Fig. 3*C*).

Given the key structural features shared between CT325 and (activated) BTZ043, it is plausible to predict that binding of the latter rests on the same key interactions—the covalent bond to Cys387 and the van der Waals interactions of the trifluoromethyl with the backbone of residues 132–134. Evidence from hexagonal crystals grown in the presence of (nominally) 3 mM BTZ043 is consistent with such reasoning. In a 2.5-Å density map, calculated with CuKα diffraction data (*BTZ-hex*; Table S1 and Fig. S6*B*), we observe distinct density peaks at the site of the trifluoromethyl group (5.5σ in the Fo-Fc difference map) and between the NO_2 group and Cys387 (6.2σ), indicating the alternative rotamer conformation of Cys387 that would facilitate the semimercaptal. Although we cannot be certain that these density features are due to a bound BTZ molecule, they align with those of the CT325 complex and are consistent with the observed saturation binding behavior of BTZ043 (Fig. S6*A*).

Overall, our structural study of DprE1 complexed with CT325 will provide a framework for the rational design of new BTZ-based inhibitors targeting *M. tuberculosis*, whereas the complex with CT319 indicates that a covalent link with DprE1 may be dispensable, provided that contacts with the disordered loop 316–322 and other parts of the active site can be exploited to enhance affinity.

Methods

Overexpression and Purification of DprE1. DprE1 (Rv3790) was coexpressed with chaperones from *E. coli* (GroES) and *M. tuberculosis* (CPN60.2) in *E. coli* BL21 (DE3). Liquid cultures of *E. coli*, harboring pET28a-*Rv3790* and pTrc-60.2-GroES, were grown at 37 °C in LB broth (Difco) supplemented with kanamycin (50 μg/mL) and ampicillin (100 μg/mL). At OD_{600nm} 0.4–0.6 the temperature was reduced to 16 °C, and protein expression of *Rv3790* and chaperones was induced by 0.5 mM isopropylthiogalactoside, followed by incubation overnight (16 °C). Cells were harvested, washed with 0.85% saline, and stored at −20 °C. Frozen cell pellets were thawed on ice and resuspended in 30 mL of 50 mM NaH_2PO_4 (pH 8), 300 mM NaCl, and 10 mM imidazole (buffer A), supplemented with EDTA-free protease inhibitor mixture (Roche). The suspension was sonicated (Sonicator Ultrasonic Liquid Processor XL; Misonix) on ice for a total time of 10 min (20-s pulses, 40-s cooling). The lysate was centrifuged (27,000 × *g*, 40 min, 4 °C), and the supernatant passed through a preequilibrated (buffer A) 1-mL Ni^{2+}-charged His-Trap column (GE Healthcare). The column was washed with 50 mL of buffer A plus 20 mM imidazole, and the protein was eluted with a 50–300 mM gradient of imidazole. Fractions containing protein were dialyzed against 20 mM Tris·HCl (pH 8.5), 10 mM NaCl, and 10% (vol/vol) glycerol (buffer B). After dialysis, the protein was loaded on a 1-mL QHP ion exchange column (Amersham), washed with 10 mL of buffer B with 50 mM NaCl, and eluted with a gradient of 20-mM NaCl steps from 100 mM to 200 mM, in buffer B. Fractions containing pure protein were dialyzed overnight against buffer B and concentrated to 35 mg/mL, by ultrafiltration (10-kDa cutoff; Amicon Ultra).

Crystallization and Structure Determination. Crystals of DprE1 were grown by sitting drop vapor diffusion in 96-well plates (Swissci), aided by a Mosquito (TTP Labtech) liquid handling robot. Conditions producing diffracting crystals of DprE1 are listed in Table S2. Crystals appeared after 1–3 d and could be mounted from the drop and frozen in liquid nitrogen without additional cryoprotection. The heavy atom derivative was obtained by immersing monoclinic crystals for 12 min in mother liquor supplemented with 50 mM ytterbium acetate, before mounting and flash freezing. Diffraction data were processed using XDS, XSCALE (21) (Table S1). Single-wavelength anomalous diffraction data from the Yb-derivative crystal (Table S1) allowed determination of the heavy atom positions [SHELXD (22)]. Heavy atom sites were refined and phases calculated [to 2.0 Å; SHARP, SOLOMON (23, 24)] (Fig. S2*A*). Autobuilding [ARPWARP (25)] produced fragments of the two molecules in the crystallographic asymmetric unit, sufficient to derive the noncrystallographic symmetry operator and enabling subsequent noncrystallographic symmetry averaging [DM (26)] (Fig. S3*B*). Placing the initial model into the unit cell of the hexagonal crystal form [PHASER (27), *Apo-hex*; Table S1] helped to complete the model of DprE1 through manual building and refinement [COOT (28), REFMAC5 (26), PHENIX.REFINE (29)]. Structures of the inhibitor-bound enzyme were solved by molecular replacement [PHASER (27)], with model building and refinement according to standard protocols. Difference maps indicating the presence of CT325 or CT319 were calculated according to protein coordinates alone, before incorporation of the ligand coordinates in the structural model. Figures were prepared using PyMol (www.pymol.org), adopting the Corey-Pauling-Koltun (CPK) coloring scheme: O, red; N, blue; S, sulfur; and C, as indicated in figure legends.

Activity Assays. The activity of DprE1, in the presence and absence of DprE2, was assayed using radiolabeled ^{14}C-DPR substrate, prepared as previously described (30). Reaction mixtures contained 50 μg of (each) enzyme, 1 mM FAD, 1mM ATP, 1 mM NAD, and 1 mM NADP, in 50 mM Mops (pH 7.9), 10 mM $MgCl_2$. To probe inhibition, enzymes were incubated with inhibitors (CT325 at 2-mM final concentration, or BTZ043 at a final concentration of 0.1 mM in 3.13% dimethyl sulfoxide) for 30 min at 30 °C, followed by addition of 2,000 cpm of ^{14}C-DPR in 5.5 μL of 1% IGEPAL. Reactions were allowed to proceed for a further 90 min and then quenched with 350 μL of $CHCl_3$:CH_3OH (2:1, vol/vol) and 55 μL H_2O. The bottom layer of the biphase was dried down, resuspended in 10 μL of $CHCl_3$:CH_3OH (2:1, vol/vol), and analyzed. Samples were spotted on to a high-performance aluminum-backed TLC plate (Merck) and separated in $CHCl_3$:CH_3OH:1M CH_3COONH_4: conc. NH_4OH:H_2O (180:140:9:9:23) (vol/vol). Bands were visualized using a phosphor imaging screen (Fuji) and a phosphor imager (Bio-Rad). CT325 was dissolved in dimethyl sulfoxide to a concentration of 2 mg/mL and added to 2 mL of tryptic soy broth in culture tubes to a final concentration between 0 and 100 μg/mL After the addition of 10 μL of a cell culture of stationary phase *M. smegmatis* mc^2155 or *M. bovis* bacillus Calmette–Guérin, the cultures were incubated at 37 °C for 40 h (*M. smegmatis*) or 10 d (*M. bovis bacillus Calmette–Guérin*) with shaking. Culture growth was monitored by measuring absorbance at 600 nm (OD_{600}) and the experiment was performed in duplicate.

Deposition of Coordinates and Structure Factors. Coordinates and structure factors of DprE1 in ligand-free and CT325-bound forms have been deposited in the Protein Data Bank (www.pdb.org).

ACKNOWLEDGMENTS. We thank Martin Day for help with recording one of the X-ray diffraction datasets, and Andy Lovering for comments on the manuscript. This work used a crystal imaging system obtained through the Birmingham Science City Translational Medicine Clinical Research and Infrastructure Trials Platform. This work was supported by Grant 084923/B/08/Z from the Wellcome Trust. G.S.B. recieves support from a Personal Research Chair from Mr. James Bardrick, and a Royal Society Wolfson Research Merit Award.

1. Manina G, Pasca MR, Buroni S, De Rossi E, Riccardi G (2010) Decaprenylphosphoryl-β-D-ribose 2′-epimerase from *Mycobacterium tuberculosis* is a magic drug target. *Curr Med Chem* 17:3099–3108.
2. Liu CH, et al. (2011) Characteristics and treatment outcomes of patients with MDR and XDR tuberculosis in a TB referral hospital in Beijing: A 13-year experience. *PLoS One* 6: e19399.
3. Gandhi NR, et al. (2010) Multidrug-resistant and extensively drug-resistant tuberculosis: A threat to global control of tuberculosis. *Lancet* 375:1830–1843.
4. Zumla A, Hafner R, Lienhardt C, Hoelscher M, Nunn A (2012) Advancing the development of tuberculosis therapy. *Nat Rev Drug Discov* 11:171–172.
5. Makarov V, et al. (2009) Benzothiazinones kill *Mycobacterium tuberculosis* by blocking arabinan synthesis. *Science* 324:801–804.
6. Pasca MR, et al. (2010) Clinical isolates of *Mycobacterium tuberculosis* in four European hospitals are uniformly susceptible to benzothiazinones. *Antimicrob Agents Chemother* 54:1616–1618.
7. Christophe T, et al. (2009) High content screening identifies decaprenyl-phosphoribose 2′ epimerase as a target for intracellular antimycobacterial inhibitors. *PLoS Pathog* 5:e1000645.
8. Mikusová K, et al. (2005) Decaprenylphosphoryl arabinofuranose, the donor of the D-arabinofuranosyl residues of mycobacterial arabinan, is formed via a two-step epimerization of decaprenylphosphoryl ribose. *J Bacteriol* 187:8020–8025.
9. Alderwick LJ, Birch HL, Mishra AK, Eggeling L, Besra GS (2007) Structure, function and biosynthesis of the *Mycobacterium tuberculosis* cell wall: Arabinogalactan and lipoarabinomannan assembly with a view to discovering new drug targets. *Biochem Soc Trans* 35:1325–1328.
10. Sassetti CM, Boyd DH, Rubin EJ (2001) Comprehensive identification of conditionally essential genes in mycobacteria. *Proc Natl Acad Sci USA* 98:12712–12717.
11. Sassetti CM, Boyd DH, Rubin EJ (2003) Genes required for mycobacterial growth defined by high density mutagenesis. *Mol Microbiol* 48:77–84.
12. Trefzer C, et al. (2010) Benzothiazinones: Prodrugs that covalently modify the decaprenylphosphoryl-β-D-ribose 2′-epimerase DprE1 of *Mycobacterium tuberculosis*. *J Am Chem Soc* 132:13663–13665.
13. Trefzer C, et al. (2012) Benzothiazinones are suicide inhibitors of mycobacterial decaprenylphosphoryl-β-D-ribofuranose 2′-oxidase DprE1. *J Am Chem Soc* 134:912–915.
14. Manina G, et al. (2010) Biological and structural characterization of the *Mycobacterium smegmatis* nitroreductase NfnB, and its role in benzothiazinone resistance. *Mol Microbiol* 77:1172–1185.
15. Forneris F, et al. (2008) Structural analysis of the catalytic mechanism and stereoselectivity in *Streptomyces coelicolor* alditol oxidase. *Biochemistry* 47:978–985.
16. Holm L, Rosenström P (2010) Dali server: Conservation mapping in 3D. *Nucleic Acids Res* 38(Web Server issue):W545-9.
17. Leferink NG, Heuts DP, Fraaije MW, van Berkel WJ (2008) The growing VAO flavoprotein family. *Arch Biochem Biophys* 474:292–301.
18. Mattevi A, et al. (1997) Crystal structures and inhibitor binding in the octameric flavoenzyme vanillyl-alcohol oxidase: The shape of the active-site cavity controls substrate specificity. *Structure* 5:907–920.
19. Udwadia ZF, Amale RA, Ajbani KK, Rodrigues C (2012) Totally drug-resistant tuberculosis in India. *Clin Infect Dis* 54:579–581.
20. Alderwick LJ, et al. (2011) Biochemical characterization of the *Mycobacterium tuberculosis* phosphoribosyl-1-pyrophosphate synthetase. *Glycobiology* 21:410–425.
21. Kabsch W (2010) Integration, scaling, space-group assignment and post-refinement. *Acta Crystallogr D Biol Crystallogr* 66:133–144.
22. Sheldrick GM (2008) A short history of SHELX. *Acta Crystallogr A* 64:112–122.
23. Schiltz M, et al. (2004) Phasing in the presence of severe site-specific radiation damage through dose-dependent modelling of heavy atoms. *Acta Crystallogr D Biol Crystallogr* 60:1024–1031.
24. Abrahams JP, Leslie AG (1996) Methods used in the structure determination of bovine mitochondrial F1 ATPase. *Acta Crystallogr D Biol Crystallogr* 52:30–42.
25. Langer G, Cohen SX, Lamzin VS, Perrakis A (2008) Automated macromolecular model building for X-ray crystallography using ARP/wARP version 7. *Nat Protoc* 3:1171–1179.
26. Collaborative Computational Project, Number 4 (1994) The CCP4 suite: Programs for protein crystallography. *Acta Crystallogr D Biol Crystallogr* 50:760–763.
27. McCoy AJ, et al. (2007) Phaser crystallographic software. *J Appl Cryst* 40:658–674.
28. Emsley P, Lohkamp B, Scott WG, Cowtan K (2010) Features and development of Coot. *Acta Crystallogr D Biol Crystallogr* 66:486–501.
29. Adams PD, et al. (2010) PHENIX: A comprehensive Python-based system for macromolecular structure solution. *Acta Crystallogr D Biol Crystallogr* 66:213–221.
30. Scherman MS, et al. (1996) Polyprenylphosphate-pentoses in mycobacteria are synthesized from 5-phosphoribose pyrophosphate. *J Biol Chem* 271:29652–29658.